Supplemental Material for "Normal-state exponential muon-spin relaxation and its implications for time-reversal symmetry breaking in Sr_2RuO_4"

Rustem Khasanov,[1,*] Thomas J. Hicken,[1] Jonas A. Krieger,[1] Maxime Lamotte,[1] Toni Shiroka,[1] Jake S. Bobowski,[2,3] Vadim Grinenko,[4] Thomas Johnson,[5,3] Naoki Kikugawa,[6] Hans-Henning Klauss,[7] Shubhankar Paul,[8,3] Benjamin M. Huddart,[9] Stephen J. Blundell,[9] Hubertus Luetkens,[1] and Yoshiteru Maeno[5,3,10,†]

[1] *PSI Center for Neutron and Muon Sciences, 5232 Villigen PSI, Switzerland*
[2] *Department of Physics, University of British Columbia, Kelowna, BC V1V 1V7, Canada*
[3] *Toyota Riken - Kyoto-Univ. Research Center (TRiKUC), Kyoto 606-8501, Japan*
[4] *Tsung-Dao Lee Institute & School of Physics and Astronomy, Shanghai Jiao Tong University, Shanghai 201210, China*
[5] *Department of Engineering, Kyoto University of Advanced Science (KUAS), Kyoto 615-8577, Japan*
[6] *National Institute for Materials Science, Tsukuba 305-0003, Japan*
[7] *Institut für Festkörper und Materialphysik, Technische Universität Dresden, 01062 Dresden, Germany*
[8] *Department of Physics, Indian Institute of Technology Kanpur, Kanpur 208016, India*
[9] *Clarendon Laboratory, University of Oxford, Department of Physics, Oxford OX1 3PU, United Kingdom*
[10] *Max Planck Institute for Chemical Physics of Solids (MPI-CPfS), Nöthnitzer Str. 40, 01187 Dresden, Germany*

(Dated: October 11, 2026)

I. SAMPLES USED FOR THE μSR EXPERIMENTS

Figure S1 shows photographs of the four Sr_2RuO_4 single crystals used in the μSR experiments and mounted on the μSR sample holders. In the main text, these crystals are denoted as samples A–D. The corresponding original labels are A (C516E2R), B (C507BC), C (C501C), and D (C140). The crystals were first mounted on a 25 μm thick copper foil, covered on top by a similar foil, with Apiezon grease in between to provide good thermal contact, and finally attached to the μSR sample holder. The sample holders have two ports, allowing two samples or reference plates to be mounted simultaneously. For samples A and B, the second port shown in Fig. S1 contains a reference high-purity Ag plate. The selected port was aligned with the muon beam by moving the cryostat vertically.

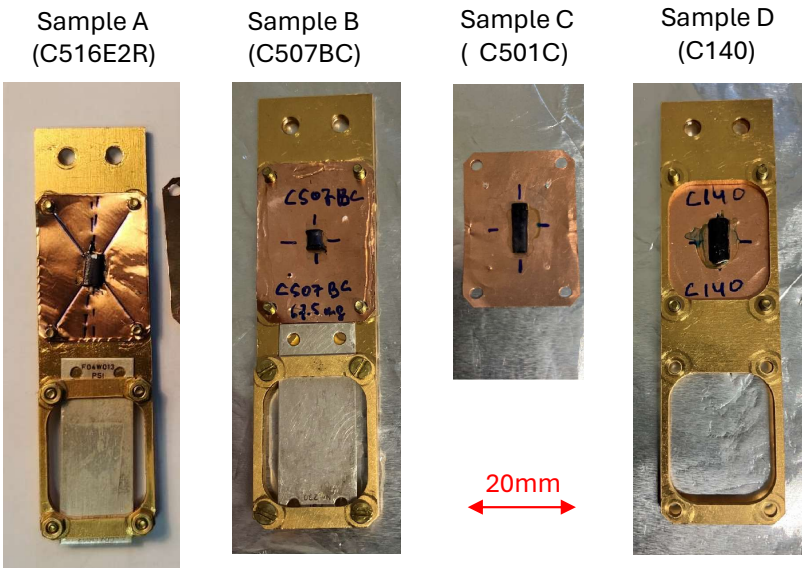


FIG. S1. Photographs of the four Sr_2RuO_4 single crystals mounted on the μSR sample holders. The original sample labels are A (C516E2R), B (C507BC), C (C501C), and D (C140). The μSR holders have two sample ports, allowing two samples or reference plates to be mounted simultaneously. The selected port was aligned with the muon beam by moving the cryostat vertically. For samples A and B, the second port contains a reference high-purity Ag plate.

* rustem.khasanov@psi.ch
† maeno.yoshiteru.b04@kyoto-u.jp

The samples have an approximately half-cylindrical shape, with the crystallographic c axis perpendicular to the cleaved surface. The approximate sample dimensions are $5 \times 3 \times 1.5$ mm^3 for sample A, $3.5 \times 3.5 \times 2$ mm^3 for sample B, $10 \times 3 \times 1.5$ mm^3 for sample C, and $7 \times 3.5 \times 1.8$ mm^3 for sample D.

The sample orientation was checked by Laue x-ray diffraction. The Laue patterns for samples A–C are shown in Fig. S2. They confirm that the crystallographic c axis is perpendicular to the cleavage plane. The crystals were glued to the copper foil with this cleavage plane facing the beam, so that the c axis was parallel to the muon momentum direction. In the TF- and LF-μSR experiments, the external magnetic field was applied along the same direction, $H \parallel c$.

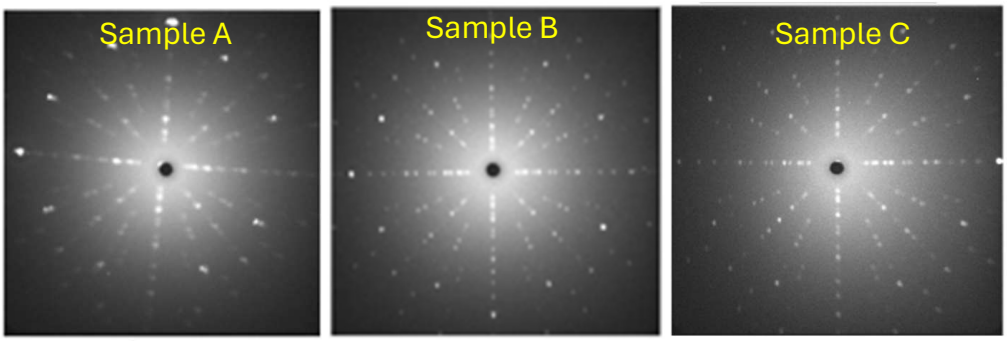


FIG. S2. Laue x-ray diffraction patterns for samples A, B, and C. The patterns confirm that the crystallographic c axis is perpendicular to the cleaved surface used for mounting the crystals on the copper foil.

The superconducting transition temperatures of samples A–C were determined from ac-susceptibility measurements. A mutual-inductance coil setup was used. The frequency and ac-field amplitude were set to 887 Hz and 8 μT, respectively. The real part of the ac response, χ', reflects the onset of diamagnetic screening, while the imaginary part, χ'', is associated with ac losses and shows a peak close to maximum absorption. We define T_c from the peak position of $\chi''(T)$. As shown in Fig. S3, this gives T_c=1.51(1), 1.48(1), and 1.40(1) K for samples A, B, and C, respectively. For sample D, T_c=1.35(2) K was taken from specific-heat measurements reported previously in Ref. 1.

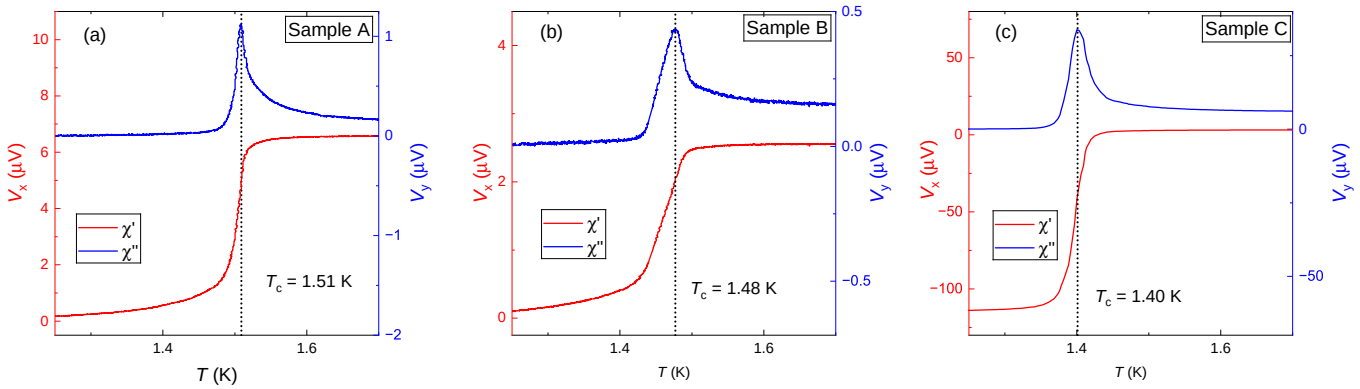


FIG. S3. Ac-susceptibility curves for (a) sample A, (b) sample B, and (c) sample C. The measured voltages V_x and V_y are proportional to the real, χ', and imaginary, χ'', parts of the ac susceptibility, respectively. The real part χ' characterizes the diamagnetic response, while χ'' represents the ac losses. The vertical dotted lines mark the superconducting transition temperatures determined from the peak positions of $\chi''(T)$: T_c=1.51(1), 1.48(1), and 1.40(1) K for samples A, B, and C, respectively.

II. DC SUSCEPTIBILITY AND IMPURITY PHASES

Figure S4 shows dc-susceptibility data, M/H, measured on pieces cut from the same parts of the growth rods as the μSR samples. The measurements were performed at $\mu_0 H = 10$ mT [panel (a)] and $\mu_0 H = 1$ T [panel (b)]. Two points should be noted. First, the dc susceptibility is expressed as the dimensionless SI volume susceptibility, where

M is the volumetric magnetization. Thus, $M/H = 10^{-4}$ corresponds to $(4\pi)^{-1} \times 10^{-4}$ emu cm^{-3} Oe^{-1} in cgs units, or approximately 4.6×10^{-4} emu mol^{-1} Oe^{-1} for Sr_2RuO_4. Second, the mass of the piece used for sample C was several times smaller than those of the other samples. We therefore normalized the sample C susceptibility to match the reported value at 300 K for fields applied parallel to the basal plane [2].

The data presented in Fig. S4 reveal sample-dependent impurity contributions. In the low-field data [Fig. S4(a)], samples A and B show a pronounced magnetic onset near 160 K, which is consistent with traces of the $SrRuO_3$ (113) phase [3, 4]. This phase is ferromagnetic and is therefore readily detected in dc magnetization. Sample C shows only a weak corresponding contribution, indicating a much smaller amount of this impurity phase.

The $\mu_0 H = 1$ T data emphasize additional lower-temperature features [Fig. S4(b)]. In particular, a broad feature or peak near 20 K is characteristic of the $Sr_3Ru_2O_7$ (327) phase, which has an enhanced magnetic susceptibility [5]. This feature is most visible in sample A, weaker in sample B, and small or absent in sample C. For sample A, we estimate impurity molar fractions of about 600 ppm for $SrRuO_3$ and 1.3% for $Sr_3Ru_2O_7$. Thus, the dc-magnetization data show that the amount and type of macroscopic impurity contribution differ substantially between the samples.

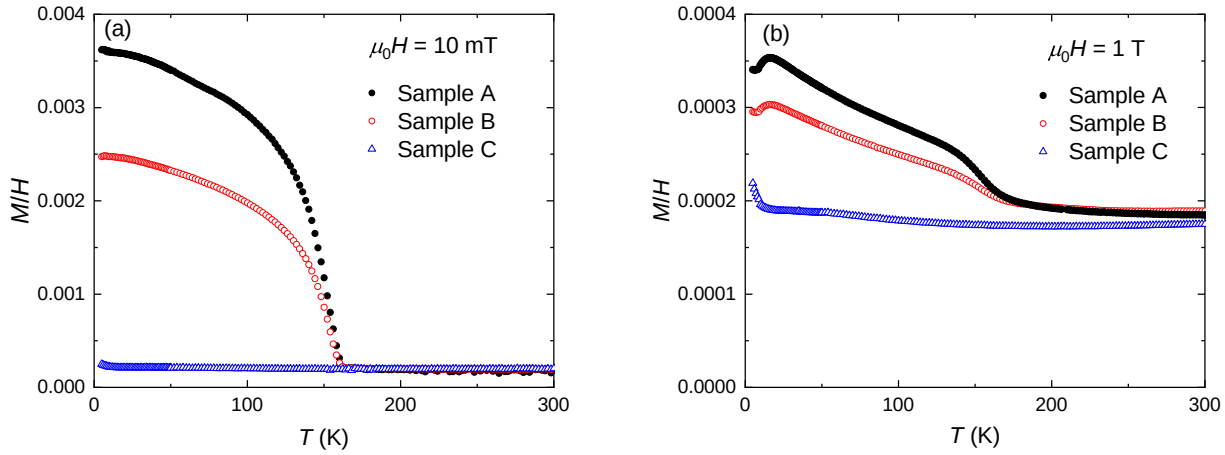


FIG. S4. DC susceptibility, M/H, measured on pieces cut from the same parts of the growth rods as the μSR samples. Panel (a) shows data measured at $\mu_0 H = 10$ mT. The magnetic onset near 160 K, observed most clearly for samples A and B, is consistent with traces of $SrRuO_3$ impurities. Panel (b) shows data measured at $\mu_0 H = 1$ T. The low-temperature feature near 20 K is characteristic of $Sr_3Ru_2O_7$ impurities and is strongest in sample A. The impurity signatures differ substantially between the samples and do not correlate with the similar low-temperature exponential μSR relaxation observed in all samples.

This impurity distribution does not correlate with the μSR relaxation. The low-temperature increase of the exponential relaxation rate is observed in all samples and has a broadly similar temperature dependence, although the dc-magnetization impurity signatures are very different. We therefore conclude that macroscopic $SrRuO_3$ or $Sr_3Ru_2O_7$ impurity phases are unlikely to be the primary origin of the exponential μSR relaxation discussed in the main text.

III. EXPERIMENTAL GEOMETRY AND DATA ANALYSIS

The experimental μSR geometry is illustrated in Fig. S5. The sample is surrounded by four detector groups, denoted Forward, Backward, Left, and Right. The incoming muon beam defines the z axis, and the sample is mounted with the crystallographic c axis parallel to this direction. The initial muon-spin polarization vector, $\mathbf{P}$, is rotated by an angle Θ with respect to the beam direction and is decomposed into a longitudinal component, $P_\parallel = |\mathbf{P}| \cos\Theta$, parallel to the z axis, and a transverse component, $P_\perp = |\mathbf{P}| \sin\Theta$, perpendicular to it. In the TF- and LF-μSR experiments, the external magnetic field was applied along the beam direction, i.e., $H \parallel c \parallel z$. The Forward/Backward detector pair is sensitive to the longitudinal component $P_\parallel$, while the Left/Right detector pair detects the transverse precession signal associated with $P_\perp$. The ZF-μSR spectra were obtained from the $P_\parallel$ component using the Forward/Backward detector pair. For a more detailed description of the μSR technique see the textbooks Refs. 6–9.

On the FLAME spectrometer, the initial muon spin was rotated by $\Theta \simeq 45°$ in xz plane, allowing both longitudinal and transverse polarization components to be recorded simultaneously. In the VMS measurements, the spin rotation was performed in the yz plane and the angle Θ was set to about 7°, corresponding effectively to an LF configuration. This small rotation was required by the weak electric field applied to the spin rotator in order to separate muons from positrons contaminating the beam.

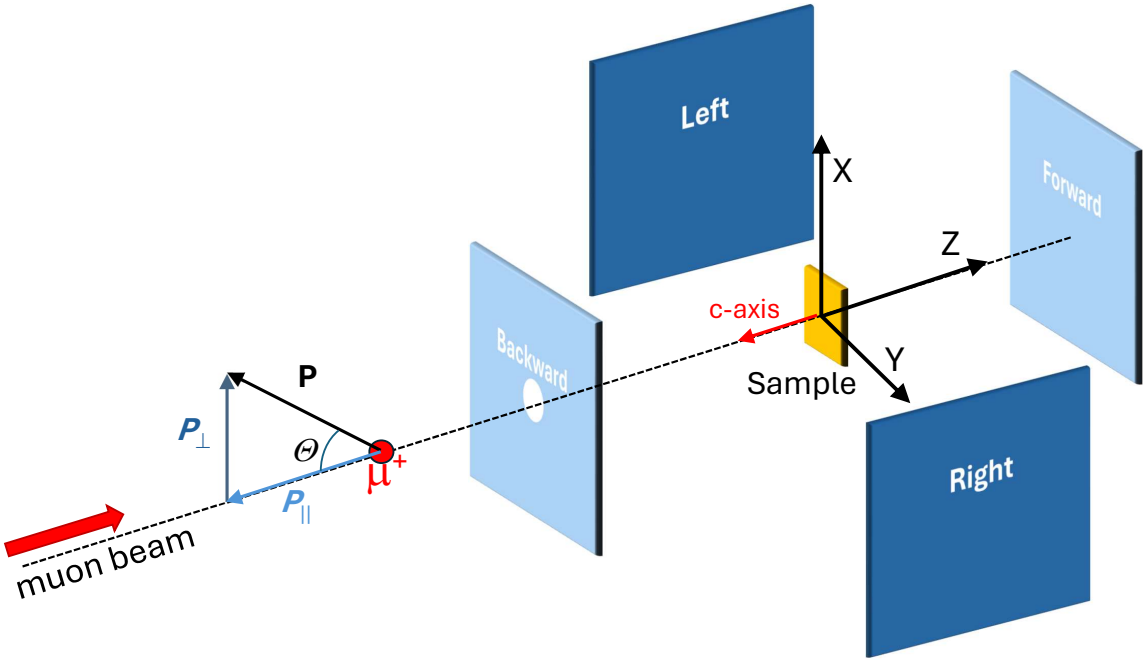


FIG. S5. Schematic measurement geometry used for the ZF-, TF-, and LF-μSR experiments. The incoming muon beam defines the z axis, and the symbol μ^+ denotes the positive muon. The sample is mounted with the crystallographic c axis parallel to the beam direction. The initial muon-spin polarization vector, $\mathbf{P}$, is rotated by an angle Θ with respect to the beam direction and is decomposed into a longitudinal component, $P_\parallel = |\mathbf{P}|\cos\Theta$, parallel to the z axis, and a transverse component, $P_\perp = |\mathbf{P}|\sin\Theta$, perpendicular to it. The detector colors indicate their use in the present analysis: the light-blue Forward and Backward detectors are used to measure the $P_\parallel$ component in ZF and LF geometries, while the dark-blue Left and Right detectors are used to measure the transverse precession signal associated with $P_\perp$ in TF geometry.

The zero-field conditions were established differently on the two spectrometers. On VMS, the residual magnetic field at the sample position was compensated using the spectrometer's automatic zero-field compensation procedure. On FLAME, active zero-field compensation was not used during the measurements. Instead, prior to the experiment, a Hall probe was placed at the sample position and the residual magnetic-field components were measured and statically compensated using the superconducting vector magnets.

IV. THE μSR DATA-ANALYSIS PROCEDURE

The dominant part of the μSR signal was attributed to the sample contribution, denoted by the subscript s. The background contribution was small compared with the sample signal and arose from muons stopping outside the sample, mainly in the copper sample holder and in the cryostat windows. Because the relaxation rates detected in the present study are weak, it was difficult to determine the background contribution precisely. Therefore, the μSR data were fitted assuming only the sample contribution, with the background contribution fixed to zero.

The time evolution of the muon-spin asymmetry was fitted as

$$A(t) = A_0 P_\mathrm{s}(t), \tag{S1}$$

where A_0 is the initial asymmetry and $P_\mathrm{s}(t)$ is the muon-spin polarization function of the sample contribution.

The sample contribution to the μSR signal was described by the following polarization functions. In ZF-μSR experiments, the sample polarization was fitted with

$$P_\mathrm{s}^\mathrm{ZF}(t) = G_\mathrm{KT}(t)\exp(-\Lambda^\mathrm{ZF}t), \tag{S2}$$

where

$$G_\mathrm{KT}(t) = \frac{1}{3} + \frac{2}{3}\left(1-\sigma_\mathrm{GKT}^2 t^2\right)\exp\left(-\frac{\sigma_\mathrm{GKT}^2 t^2}{2}\right)$$

is the static Gaussian Kubo-Toyabe relaxation function, and σ_{GKT} is the Gaussian relaxation rate associated mainly with nuclear magnetic moments. For TF-μSR experiments, the sample contribution was described by

$$P_{\mathrm{s}}^{\mathrm{TF}}(t) = \exp\left[-\frac{(\sigma^{\mathrm{TF}})^2 t^2}{2}\right] \exp(-\Lambda^{\mathrm{TF}} t)\cos(\gamma_\mu B_{\mathrm{int}} t + \phi), \tag{S3}$$

while for LF-μSR experiments it was described by

$$P_{\mathrm{s}}^{\mathrm{LF}}(t) = \exp(-\Lambda^{\mathrm{LF}} t). \tag{S4}$$

Here Λ and σ denote the exponential and Gaussian relaxation rates, respectively, $\gamma_\mu = 2\pi \times 135.5$ MHz/T is the muon gyromagnetic ratio, B_{int} is the internal magnetic field at the muon stopping site, and ϕ is the initial phase of the muon-spin ensemble. The superscripts ZF, TF, and LF denote quantities obtained in zero-field, transverse-field, and longitudinal-field μSR experiments, respectively.

V. ADDITIONAL ZERO-FIELD μSR DATA

Figure S6 shows representative ZF-μSR spectra for samples A–D measured at 2 K and at base temperature. The base temperature was 50 mK for sample A and 40 mK for samples B–D. The low-temperature spectra relax more rapidly than the 2 K spectra, demonstrating directly the low-temperature enhancement of the relaxation. The ZF-μSR data were fitted using Eq. (S1) with the sample contribution described by Eq. (S2).

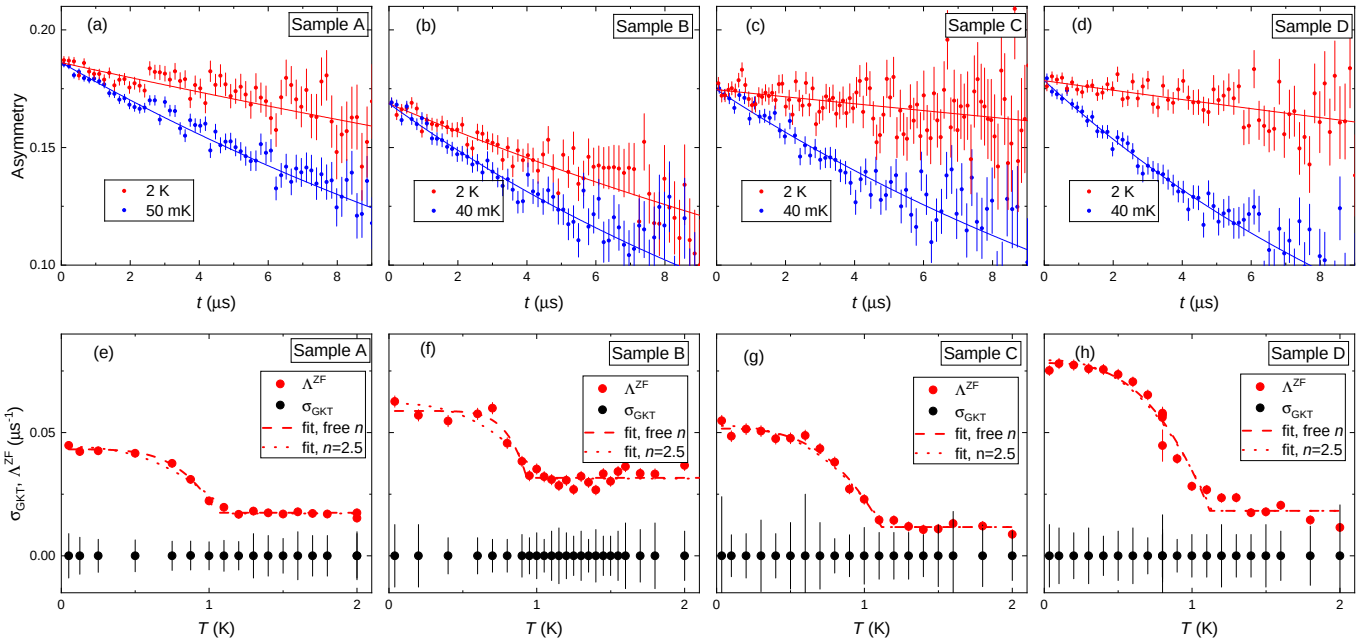


FIG. S6. ZF-μSR data for samples A–D. Panels (a)–(d) show representative asymmetry spectra measured at 2 K and at base temperature: 50 mK for sample A and 40 mK for samples B–D. Solid lines are fits using Eq. (S1) with the ZF polarization function given in Eq. (S2). Panels (e)–(h) show the temperature dependences of Λ^{ZF} and σ_{GKT} obtained from fits in which both parameters were allowed to vary. The dashed curves are fits of $\Lambda^{\mathrm{ZF}}(T)$ to Eq. (1) of the main text with n varied freely, while the dotted curves are fits with fixed $n = 2.5$. The corresponding fit parameters are listed in Table S1.

The lower panels of Fig. S6 show the temperature dependences of the exponential relaxation rate Λ^{ZF} and the Gaussian Kubo-Toyabe relaxation rate σ_{GKT} obtained from fits in which both parameters were allowed to vary. Fits reveal that σ_{GKT} remains small and is consistent with zero, while the low-temperature increase is carried by Λ^{ZF}. This does not imply the absence of nuclear magnetic moments. Rather, it means that, for the present data and fitting range, a separate temperature-dependent Gaussian Kubo-Toyabe contribution is not resolved and the additional low-temperature relaxation is better represented by an exponential term. The temperature dependence of Λ^{ZF} was fitted by Eq. (1) of the main text in two ways: with the exponent n varied freely and with fixed $n = 2.5$. The latter value represents a common average exponent for the ZF and 80 mT TF data sets and is used to reduce correlations between the fit parameters. The resulting parameters are summarized in Table S1. For the ZF data discussed in the main text, σ_{GKT} was fixed to zero and Λ^{ZF} was used as the relevant temperature-dependent parameter.

VI. COMPARISON OF ZF-μSR DATA MEASURED ON FLAME AND VMS

To check whether the ZF relaxation enhancement is related to a particular spectrometer, ZF-μSR measurements on sample B were performed on both the FLAME and VMS instruments at PSI. The comparison is shown in Fig. S7. Both data sets show a low-temperature increase of the exponential relaxation rate, with similar onset temperatures obtained from fits to Eq. (1) of the main text: $T_\Lambda = 1.04(6)$ K for FLAME and $T_\Lambda = 1.17(7)$ K for VMS.

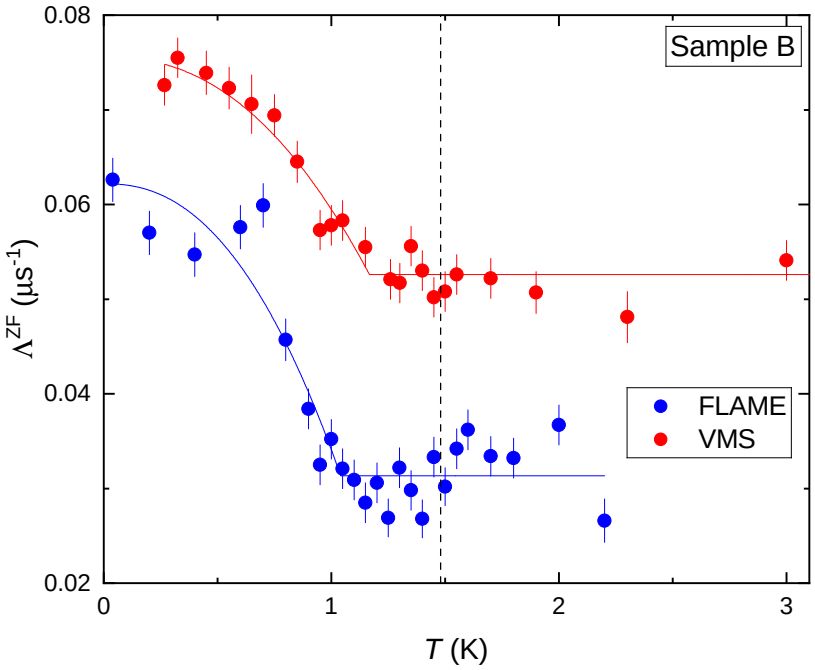


FIG. S7. Comparison of the ZF-μSR exponential relaxation rate measured on sample B using the FLAME and VMS spectrometers at PSI. Solid lines are fits to Eq. (1) of the main text. Both data sets show a low-temperature increase of Λ^{ZF}, although the absolute offset and relaxation amplitude differ slightly between the instruments.

The absolute values of the fit parameters differ somewhat between the two instruments. In particular, the VMS data show a larger temperature-independent offset Λ_0 and a slightly different relaxation enhancement $\Delta\Lambda$. These differences are most likely caused by different spectrometer backgrounds. For sample B, such background contributions are affected by the relatively small sample dimensions perpendicular to the beam direction, approximately 3.5×3.5 mm^2; see also Fig. S1. This effect persists despite the use of veto mode on both instruments. The important point is that the low-temperature increase of Λ^{ZF} occurs at nearly the same temperature on both instruments, ruling out a simple spectrometer-specific artifact as the origin of the effect.

VII. ADDITIONAL TRANSVERSE-FIELD μSR DATA

A. TF-μSR at 80 mT

Figure S8 shows representative TF-μSR asymmetry spectra measured at 80 mT for samples A–C. The spectra were fitted using Eq. (S1) with the TF sample polarization function given in Eq. (S3). At this field, bulk superconductivity is suppressed for all three samples, as discussed in the main text.

The lower panels of Fig. S8 show the temperature dependences of Λ^{TF} and σ^{TF} obtained from fits in which both parameters were allowed to vary. The Gaussian relaxation rate is small and remains close to zero within the experimental uncertainty. The temperature-dependent relaxation is therefore captured by the exponential rate Λ^{TF}. The temperature dependence of Λ^{TF} was fitted by Eq. (1) of the main text using the same two procedures as for the ZF data, namely with n varied freely and with fixed $n = 2.5$. The corresponding fit parameters are listed in Table S1. Consequently, the 80 mT TF data presented in the main text were fitted with σ^{TF} fixed to zero. This procedure provides a direct comparison between the normal-state TF relaxation channel and the ZF exponential relaxation discussed in the main text.

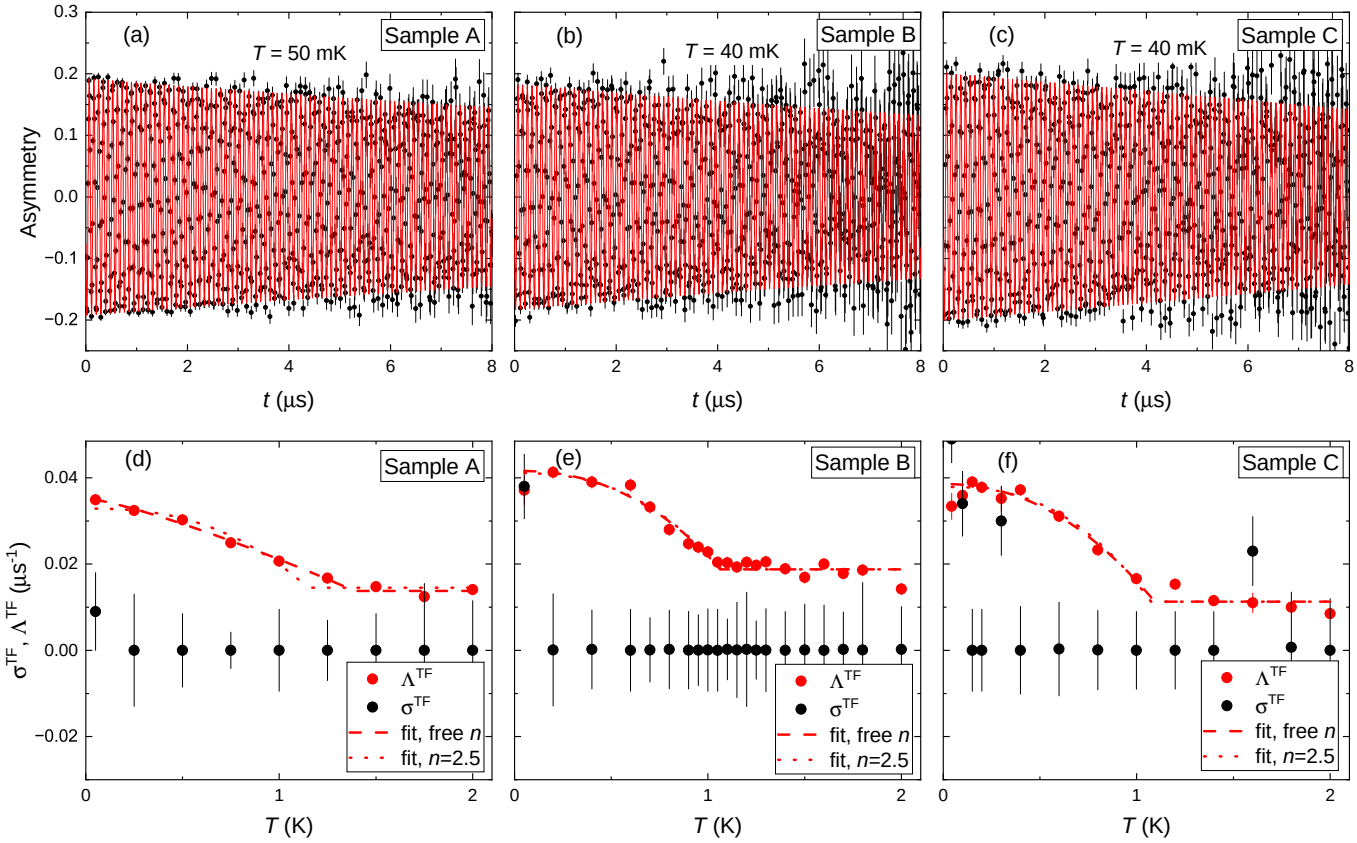


FIG. S8. TF-μSR data measured at 80 mT for samples A–C. Panels (a)–(c) show representative asymmetry spectra at base temperature. Solid lines are fits using Eq. (S1) with the TF polarization function given in Eq. (S3). Panels (d)–(f) show the temperature dependences of Λ^{TF} and σ^{TF} obtained from fits in which both parameters were allowed to vary. The dashed curves are fits of $\Lambda^{\mathrm{TF}}(T)$ to Eq. (1) of the main text with n varied freely, while the dotted curves are fits with fixed $n = 2.5$. The corresponding fit parameters are listed in Table S1.

B. TF-μSR below $H_{c2}^{\parallel c}(0)$

In TF-μSR measurements with the applied field below $H_{c2}^{\parallel c}(0)$, the sample enters the superconducting mixed state on cooling below the field-dependent transition temperature $T_c(H)$. This transition is detected by the onset of the Gaussian relaxation σ^{TF}, which reflects the inhomogeneous field distribution of the flux-line lattice, and by the corresponding change in the internal field B_{int}.

Figure S9 illustrates the procedure used to determine $T_c(H)$ for samples A–C in a transverse field of 45 mT. The arrows mark $T_c(H)$, defined as the temperature at which $\sigma^{\mathrm{TF}}(T)$ and $B_{\mathrm{int}}(T)$ start to deviate from their normal-state behavior. The exponential relaxation rate Λ^{TF} shows a separate low-temperature increase below a characteristic temperature denoted $T^*(H)$. This temperature lies below $T_c(H)$ and should therefore not be identified directly with the superconducting transition itself.

The appearance of T^* only in fields below $H_{c2}^{\parallel c}(0)$ suggests that it is connected with the superconducting mixed state. A natural possibility is an additional change in the vortex-state field distribution, for example a rearrangement of the flux-line lattice or an additional low-temperature broadening. This contribution is distinct from the 80 mT normal-state relaxation channel, which is present even when bulk superconductivity is suppressed. Thus, below $H_{c2}^{\parallel c}(0)$, the measured exponential relaxation contains both the normal-state channel and an additional superconducting mixed-state contribution.

Figure S10 compares T_Λ from ZF-μSR and $T^*(H)$ values extracted from TF-μSR measurements below $H_{c2}^{\parallel c}(0)$ with $T_c(H)$. For all three samples, both temperature scales remain below the corresponding superconducting transition temperature. The data suggest an approximately parallel offset of these scales from T_c, but the present measurements do not establish whether T_Λ and T^* have the same microscopic origin. In the main text we therefore treat T_Λ as the onset of the phenomenological exponential relaxation in ZF, while T^* is used to denote the additional low-temperature

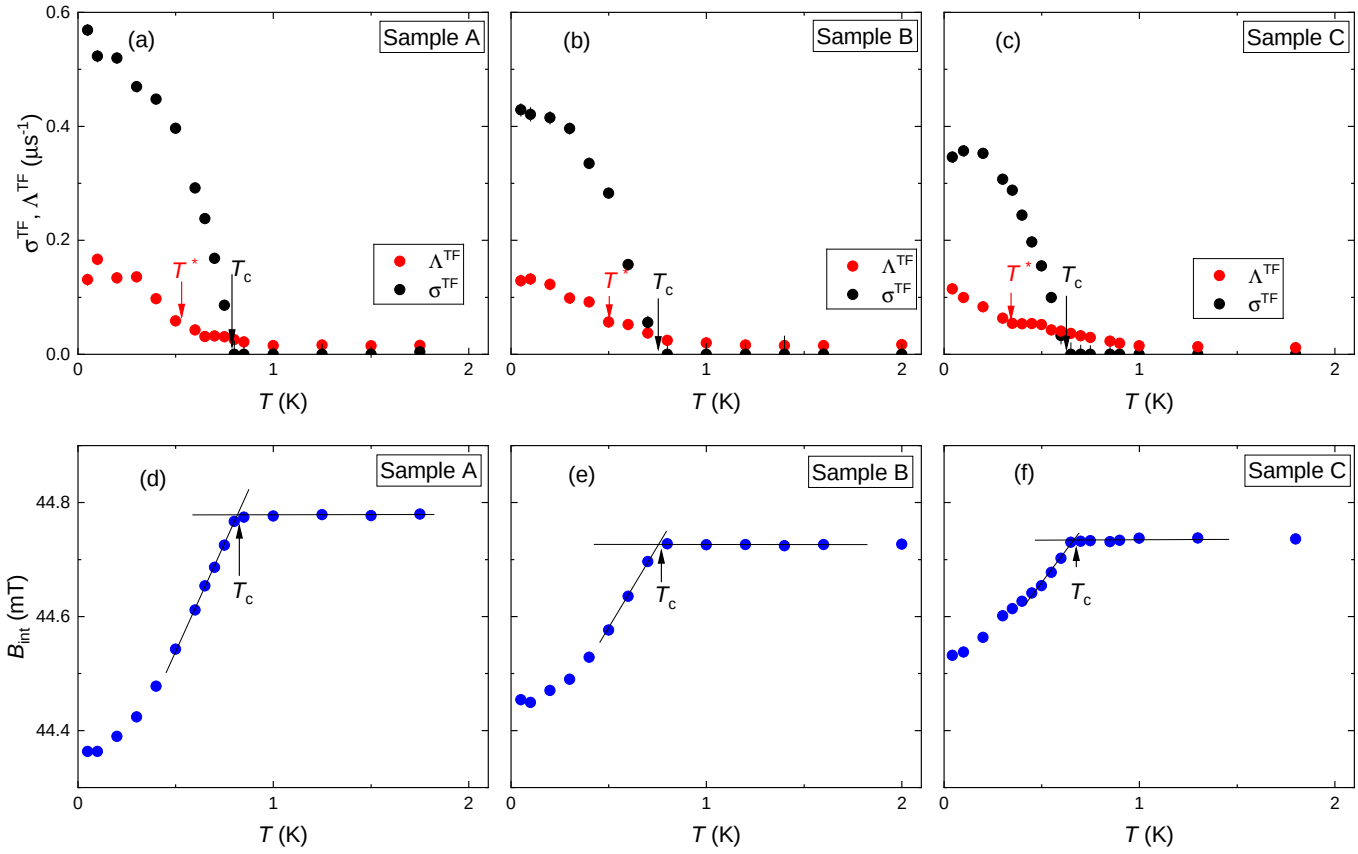


FIG. S9. TF-μSR data measured in an applied field of 45 mT for samples A–C. Panels (a)–(c) show the temperature dependences of σ^{TF} and Λ^{TF}. Panels (d)–(f) show the corresponding temperature dependences of the internal field B_{int}. The arrows indicate the superconducting transition temperature $T_{\mathrm{c}}(H)$, determined from the onset of σ^{TF} and the change of B_{int}. The temperature $T^*(H)$ marks the low-temperature increase of Λ^{TF} within the superconducting mixed state.

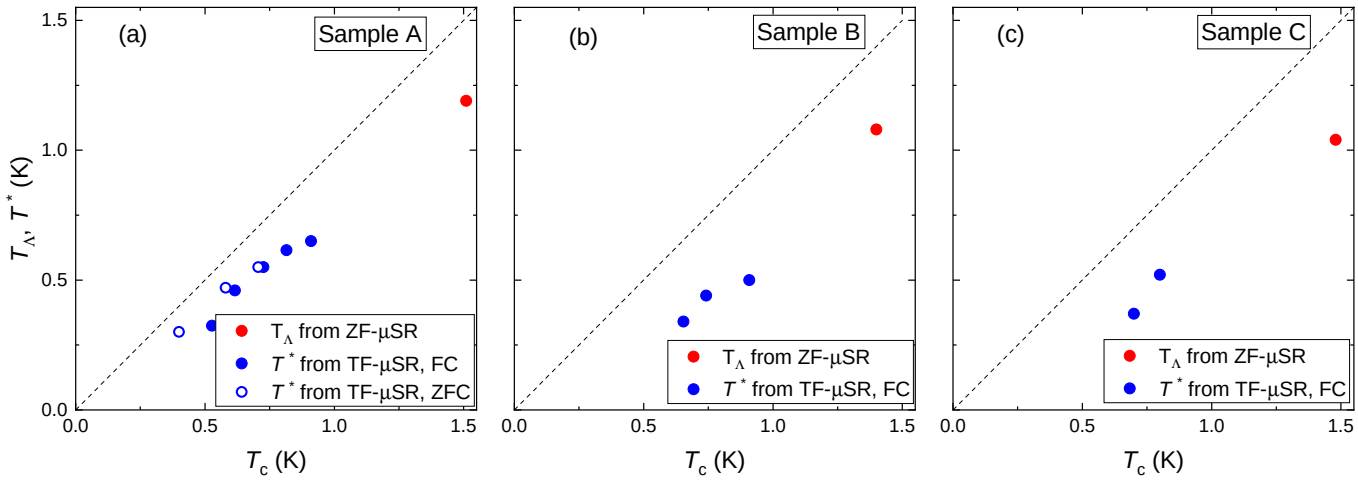


FIG. S10. Comparison of T_Λ obtained from ZF-μSR and $T^*(H)$ obtained from TF-μSR measurements below $H_{c2}^{\parallel c}(0)$ with $T_{\mathrm{c}}(H)$ for (a) sample A, (b) sample B, and (c) sample C. The dashed line corresponds to $T_\Lambda = T_{\mathrm{c}}$ or $T^*(H) = T_{\mathrm{c}}(H)$. Both temperature scales lie below the superconducting transition temperature.

relaxation observed in the superconducting mixed state.

C. Fit parameters for ZF and 80 mT TF relaxation

The parameters obtained from fits of the $\Lambda^{\mathrm{ZF}}(T)$ and $\Lambda^{\mathrm{TF,80mT}}(T)$ data using Eq. (1) of the main text are summarized in Table S1. Two cases were considered: (i) fits with the power-law exponent n varied freely, shown in the upper part of the table, and (ii) fits with fixed $n = 2.5$, shown in the lower part. The latter procedure reduces correlations between the fit parameters entering Eq. (1).

TABLE S1. Fit parameters obtained from Eq. (1) of the main text for the ZF and 80 mT TF exponential relaxation rates. Here T_Λ is the onset temperature of the relaxation enhancement, $\Delta\Lambda$ is the low-temperature increase of the exponential relaxation rate Λ, Λ_0 is the high-temperature relaxation rate, and n is the phenomenological power-law exponent. The upper part shows fits with n varied freely, while the lower part shows fits with fixed $n = 2.5$. For sample D, only ZF-μSR data are available.

Sample	Experiment	T_Λ (K)	$\Delta\Lambda$ (μs^{-1})	Λ_0 (μs^{-1})	n
		Free exponent n			
A	ZF	1.05(7)	0.026(2)	0.017(2)	4.2(6)
	TF 80 mT	1.39(8)	0.021(2)	0.014(2)	1.3(2)
B	ZF	0.94(7)	0.027(3)	0.032(1)	6.8(3.0)
	TF 80 mT	1.07(9)	0.023(2)	0.019(2)	2.3(6)
C	ZF	1.12(7)	0.040(4)	0.012(2)	3.0(4)
	TF 80 mT	1.09(8)	0.027(3)	0.011(2)	2.2(6)
D	ZF	1.12(7)	0.060(3)	0.018(2)	2.8(4)
		Fixed exponent $n = 2.5$			
A	ZF	1.14(6)	0.027(2)	0.017(2)	2.5 fixed
	TF 80 mT	1.15(7)	0.018(2)	0.014(2)	2.5 fixed
B	ZF	1.04(6)	0.030(2)	0.031(2)	2.5 fixed
	TF 80 mT	1.06(7)	0.022(2)	0.019(2)	2.5 fixed
C	ZF	1.14(6)	0.041(3)	0.012(2)	2.5 fixed
	TF 80 mT	1.07(6)	0.022(2)	0.011(2)	2.5 fixed
D	ZF	1.13(5)	0.061(3)	0.018(2)	2.5 fixed

VIII. ADDITIONAL LONGITUDINAL-FIELD μSR DATA

The LF-μSR asymmetry spectra measured on sample B are shown in Fig. S11. The data were fitted using Eq. (S1) with the LF polarization function given in Eq. (S4). Panel (a) shows the data at 2 K, i.e., above T_c. In this normal-state measurement, increasing the longitudinal field suppresses the relaxation, as expected for decoupling from a static or quasistatic local-field distribution.

Panel (b) shows the data at 50 mK, i.e., in the superconducting state. In this case, the relaxation increases with increasing applied field up to 2 mT. This behavior is opposite to the conventional normal-state decoupling trend and indicates that an additional source of transverse local-field components appears in the superconducting state. As discussed in the main text, partial diamagnetism, vortex penetration, demagnetization effects, and geometrical barriers can distort the internal field distribution in a finite rectangular sample. Therefore, even in nominal LF geometry, the local field at the muon stopping site can acquire a component perpendicular to the initial muon-spin polarization and contribute to the relaxation.

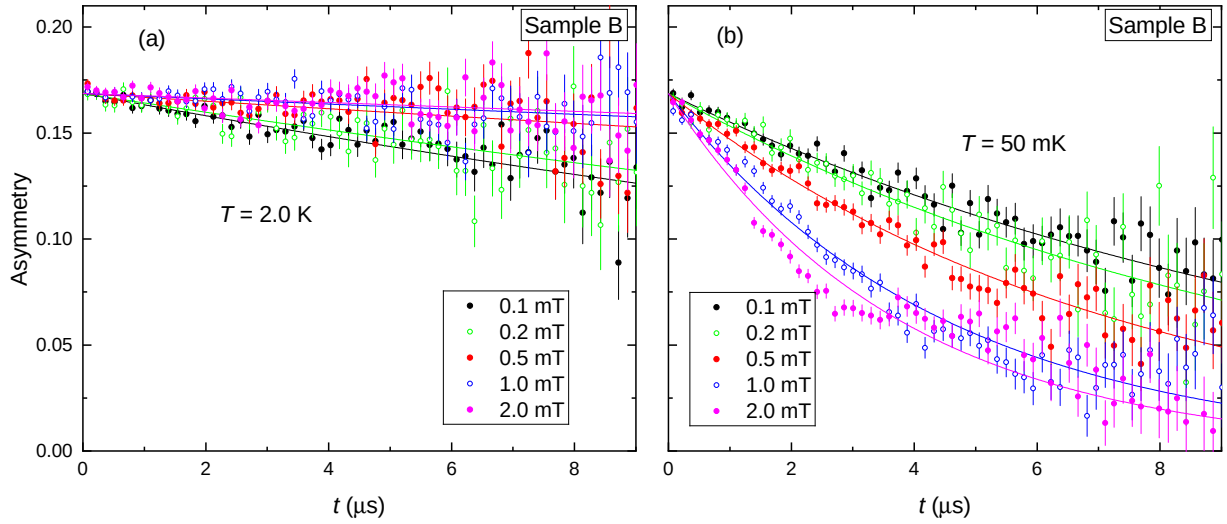


FIG. S11. LF-μSR asymmetry spectra measured on sample B (a) above T_c at 2 K and (b) below T_c at 50 mK. The applied longitudinal fields are indicated in the figure. Solid lines are fits using Eq. (S1) with the LF polarization function given in Eq. (S4).

IX. MUON STOPPING SITES, NUCLEAR RELAXATION, AND MUON HOPPING

A. Muon stopping sites and zero-point energy

We have carried out density functional theory (DFT) calculations using the plane-wave basis-set electronic structure code CASTEP [10] to determine the muon stopping sites. Calculations were carried out within the generalized-gradient approximation (GGA) using the PBE functional [11], treating the system as non-spin-polarized. Sr_2RuO_4 crystallizes in the centrosymmetric $I4/mmm$ (No. 139) space group, with $a = b = 3.871$ Å and $c = 12.702$ Å [12]. Convergence testing was carried out on a conventional Sr_2RuO_4 unit cell; a plane-wave cutoff energy of 900 eV and $9 \times 9 \times 3$ Monkhorst-Pack grid [13] for Brillouin zone sampling resulted in total energies that converge to within 1 meV per atom.

Muon site calculations were carried out using the MuFinder program [14]. Initial structures comprising a muon (modeled as a proton) and a $3\times3\times1$ Sr_2RuO_4 supercell were generated by requiring the muon to be at least 0.5 Å away from each of the initial muon positions in the previously generated structures (including their symmetry equivalent positions) and at least 1.0 Å away from any of the atoms in the cell. The larger cell dimensions meant that we instead used a $3 \times 3 \times 3$ Monkhorst-Pack grid for these calculations, providing equivalent k-point density to the $9 \times 9 \times 3$ grid identified in our convergence testing on a single unit cell. This resulted in 36 structures which were subsequently allowed to relax until the calculated forces on the atoms were all $< 5 \times 10^{-2}$ eV Å^{-1} and the total energy and atomic positions converged to within 2×10^{-5} eV per atom and 1×10^{-3} Å, respectively.

These structural relaxations result in five crystallographically distinct candidate muon stopping sites. The lowest energy cluster of sites (comprising 26 structures) is consistent with the muon stopping site proposed in Ref. [15]. For this site, denoted site A, the muon sits approximately 0.97 Å from an apical oxygen of a RuO_6 octahedron. Representative sites from each class were further re-relaxed with a tighter force tolerance of 1×10^{-2} eV Å^{-1}, both with and without the symmetry of the site imposed. One candidate relaxed into site A in both cases. Its original relaxation had stopped on a nearly flat shelf, where the residual force fell just below the default threshold, so it is neither a stable site nor a transition state. A second candidate survived only when its symmetry was imposed; without it, it also relaxed into site A. This is therefore a saddle point, which we label X. X involves a muon sitting 0.97 Å from an apical oxygen, and is related to site A by rotating the μ–O bond by 45° about the Ru–O axis, placing it midway between two symmetry-equivalent copies of site A. This leaves three stable crystallographically distinct muon stopping sites, which we show in Table S2. Sites B and C are consistent with the corresponding sites in the Supplementary Material of Ref. [15]. However, these are ≈ 1 eV or higher in energy than the lowest-energy site and are therefore unlikely to be occupied in practice.

Although the calculations identify only one energetically relevant low-energy muon stopping site, site A has Wyckoff position 16n and therefore corresponds to multiple symmetry-equivalent physical positions within the unit cell. We therefore need to consider the possibility that the muon is able to move between these positions. This is illustrated

TABLE S2. Muon stopping sites and saddle points in Sr_2RuO_4. Positions are given in fractional coordinates within the conventional cell, relative to the host lattice, i.e. corrected for small rigid shifts of the host ($\leq$ 0.04 Å) arising during the relaxations. Energies are given relative to the lowest-energy site.

	Fractional coordinates	Energy (eV)
A	(0.000, 0.229, 0.185)	0.000
B	(0.264, 0.437, 0.000)	0.978
C	(0.000, 0.500, 0.250)	1.677
X	(0.144, 0.144, 0.195)	0.070
Y	(0.000, 0.500, 0.101)	0.675
Z	(0.250, 0.250, 0.250)	0.754

TABLE S3. Harmonic Γ-point modes of the muon in Sr_2RuO_4, from a finite-displacement phonon calculation. The muon share is the squared norm of the mode eigenvector projected onto muon motion.

Mode	$\hbar\omega/2$ (eV)	Muon share	Character
1	0.137	0.997	Bend about the Ru–O axis
2	0.139	0.995	Bend in the Ru–O–μ plane
3	0.646	0.993	O–μ stretch

in Fig. 7 of the main text, where we show candidate hopping paths between symmetry-equivalent replicas of site A. Determining whether these paths are accessible requires comparing the energy barriers between these sites with the zero-point energy of the muon.

In the weakly bound adiabatic limit (i.e., with zero entanglement with nearby nuclear positions) [16], the zero-point energy (ZPE) of the muon can be approximated as the sum of the three highest-frequency phonon modes. These were calculated at the Γ point using the finite displacement method and are reported in Table S3. The entanglement witness w_1, obtained by projecting the three highest-energy (normalized) phonon normal modes onto pure muon motion, summing the squared norms of the resulting (projected) phonon eigenvectors, and subtracting the upper bound 3 [16], can be used to determine whether the muon is in fact in this limit. This results in $w_1 = 0$ for zero muon-nuclear entanglement (weakly bound adiabatic limit) and $w_1 < 0$ in the entangled, many-body case. Here we obtain $w_1 = -0.014$, which is close to zero, confirming the validity of the weakly bound adiabatic approximation, i.e., the decoupling of muon vibrational modes from the vibrational modes of the lattice. Notably, a finite-displacement calculation in which only the muon is displaced, with the host held fixed, gives a muon ZPE of 0.918 eV, within 4 meV of the 0.922 eV obtained from the full phonon calculation on the same structure, and essentially identical eigenvectors. This reflects the large separation between the muon modes and the host phonon band. Subsequent muon ZPEs were therefore obtained from frozen-host calculations, which require only three perturbations rather than 255 and so significantly reduce the computational cost.

B. Nuclear contribution to the zero-field relaxation

The exponential relaxation observed in ZF-μSR, including the finite relaxation present above T_c, is reproducible between measurements on different samples. Its decoupling by modest longitudinal fields points to a predominantly static or quasistatic origin. One possible source of such local fields is the nuclear moments. Oxygen has no nuclear moment apart from the 0.04% natural abundance of ^{17}O, whereas ^{87}Sr, ^{99}Ru, and ^{101}Ru have finite nuclear moments and natural abundances of approximately 7%, 13%, and 17%, respectively. The remaining isotopes have $I = 0$, giving a relatively dilute distribution of nuclear spins.

We simulated the effect of these static nuclear moments at the calculated muon site using a Monte Carlo method, averaging over many random configurations of the naturally abundant magnetic isotopes. The result is shown in Fig. S12. The calculated relaxation is much closer to a Gaussian-like form than to the experimentally observed exponential relaxation and is also far too weak to account for its magnitude.

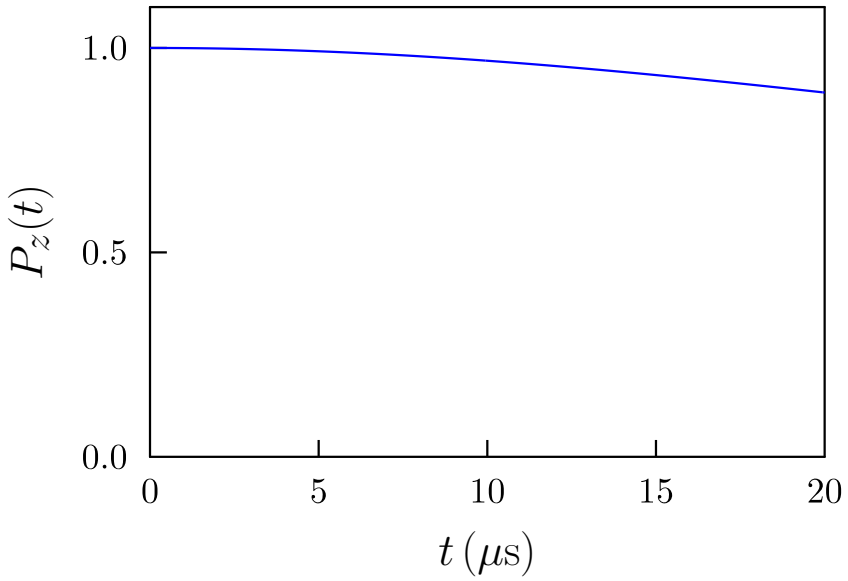


FIG. S12. Simulated zero-field relaxation expected from static nuclear moments at the calculated muon site. The calculation includes the natural abundances of the magnetic O, Ru and Sr isotopes and was evaluated by averaging over many random isotope configurations.

C. Muon hopping paths and zero-point-corrected barriers

To identify possible muon hopping paths, we considered all pairs of symmetry-equivalent muon sites separated by less than 3.0 Å. This resulted in the five candidate paths shown in Fig. 7 of the main text. Initial guesses for the transition states can be obtained using symmetry arguments. We start by considering path P1. The start and end points of this path are related by the mirror plane m as shown in Fig. S13(a). A symmetric transition state must therefore be a minimum within this plane. We have already identified this state: it is X from our structural relaxations, corresponding to an energy barrier of 70 meV. Next consider P2. Any path between muon sites on opposite sides of the apical O either crosses the fourfold rotation axis through the O, as shown by the orange path in Fig. S13(a), or goes around it. Along this axis, the muon has a Sr atom above it and an O atom below it, so we would expect there to be a minimum along this axis that puts the muon at a distance of around 1 Å from the O. At this point the fourfold rotation symmetry means that the two in-plane curvatures must be equal. If these curvatures are both positive, then the minimum along this axis would be a minimum in all directions, i.e. a muon site. However, such a site was not identified among our relaxed structures, suggesting that this point is instead an in-plane maximum. Hence, the minimum energy path between these muon sites should avoid this axis, instead crossing both mirror planes m, whose minima correspond to X. Path P2 is therefore not a distinct path, but is instead achieved by traversing two equivalent P1 paths in succession.

Because of the muon's small mass, its ZPE can differ significantly between its site and the transition state. Within zero-point-corrected harmonic transition-state theory, this gives a corrected barrier [17, 18]

$$\Delta E_{\mathrm{corr}} = \Delta E + \sum_i \tfrac{1}{2}\hbar\omega_i^{\mathrm{s}} - \sum_i \tfrac{1}{2}\hbar\omega_i^{\mathrm{A}}, \tag{S5}$$

where the sums run over the real muon vibrational modes, with frequencies ω_i^{s} and ω_i^{A} at the saddle and at site A, respectively. The muon-only Hessian at X (host held fixed) has a single imaginary mode: the bend about the Ru–O axis, along the minimum-energy path. Allowing the host to respond to the muon displacement can only lower the effective muon curvatures, so this instability persists, while the two remaining modes are too stiff (3.4 and 46.9 eV Å^{-2}) to be destabilized, confirming that X is a first-order saddle point. These modes, the in-plane bend and the O–μ stretch, are 28% and 2% higher in frequency than at site A, giving a ZPE of 0.835 eV compared with 0.918 eV at site A. With $\Delta E = 0.070$ eV, the corrected barrier for P1 is -0.013 eV, i.e. effectively zero within the harmonic approximation. Since P2 is two successive P1 hops, the muon can move freely among the four equivalent A sites around the same apical oxygen.

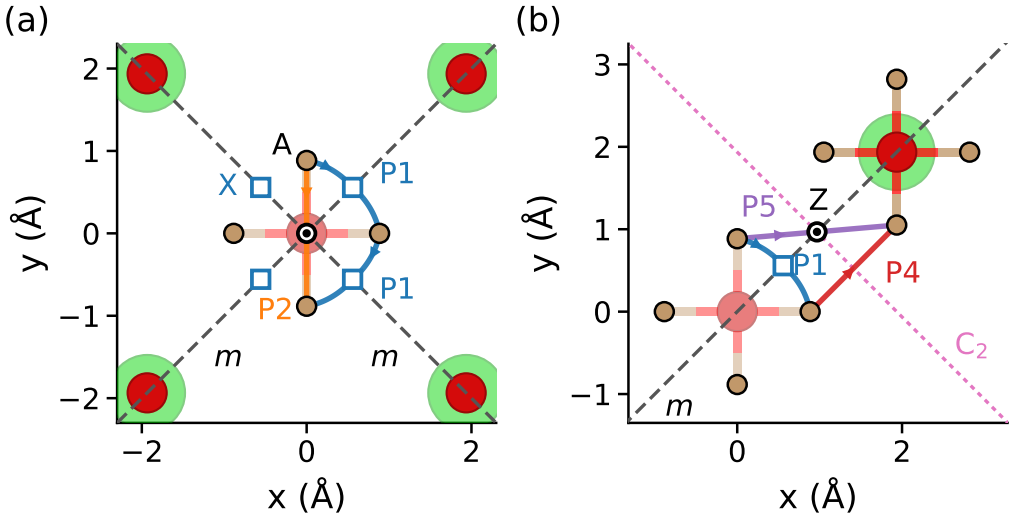


FIG. S13. (a) Candidate hopping paths between sites involving muons bonded to the same apical O atom. Open squares represent point X from our structural relaxations, which lies on the diagonal mirror plane m. P1 (blue) passes through it and two successive P1 hops connect muons on opposite sides of the apical O atom. A direct path P2 (orange) connecting these muons would instead cross the fourfold rotation axis through the O. (b) Paths joining muons bonded to apical O atoms in adjacent SrO layers. P4 and P5 share an endpoint, and their starting points are one P1 hop apart. Z is a candidate transition state for both paths and lies at the intersection of a twofold rotation axis C_2 and a mirror plane m.

For path P3, the ends of the path are exchanged by a twofold axis along $(0, 1/2, z)$, so a symmetric transition state must lie on this line. Relaxing the muon along this line from the midpoint of the path ($z = 0.185$) led to site C. However, an earlier relaxation seeded close to the line at $z = 0.104$ moved down to $z \approx 0.093$ before escaping transversely into site A, indicating a second minimum lower on the line. Restarting the constrained relaxation from $z = 0.093$, the muon converged at $z = 0.101$, bonded to an equatorial oxygen, 0.675 eV higher in energy than site A. This point, Y, is a minimum along the line but unstable to transverse displacement, and is therefore the transition state of P3. Unlike X, all three muon modes at Y remain real when the host is held fixed, so the instability seen in the relaxations must arise from relaxation of the host. All three modes therefore contribute to the ZPE at Y (0.915 eV), giving a corrected barrier of 0.671 eV.

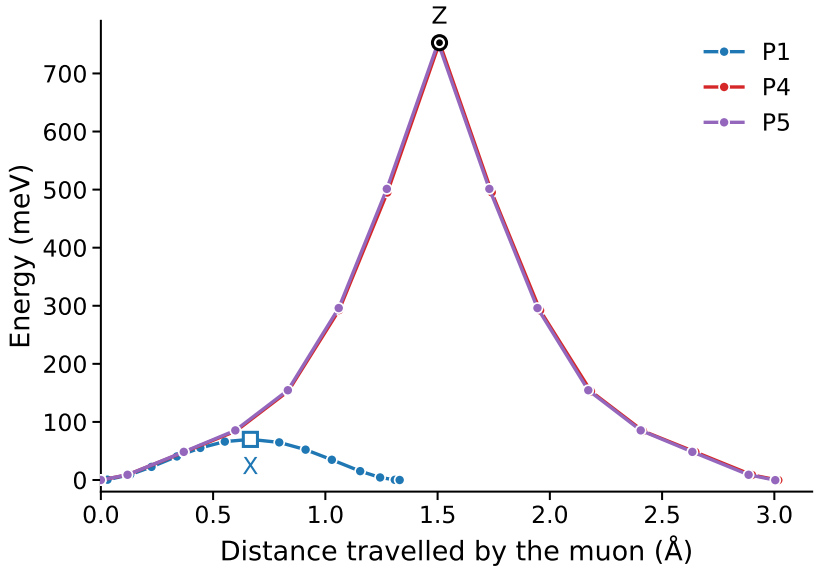


FIG. S14. Energy profiles along paths P1, P4 and P5 from climbing-image nudged elastic band (NEB) calculations, relative to site A, as a function of the distance traveled by the muon (measured relative to the host center of mass). The maxima coincide with the saddle points X (P1) and Z (P4 and P5).

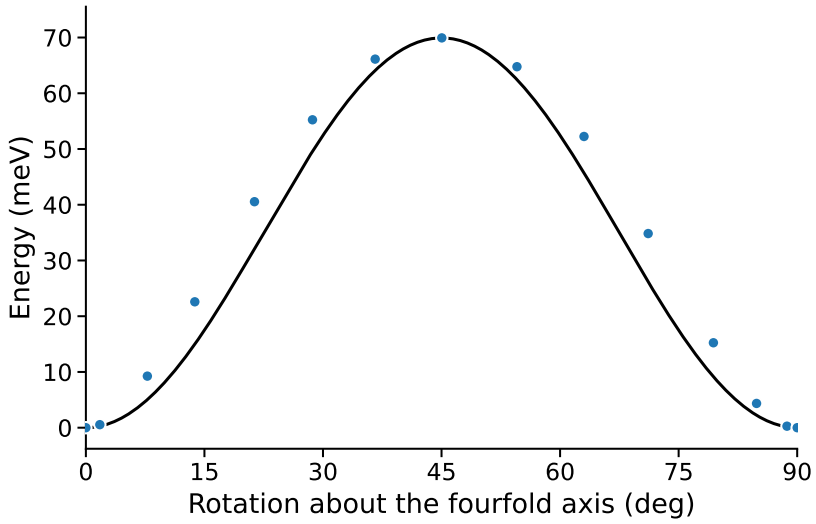


FIG. S15. Energy barrier between the two closest symmetry-related copies of the muon site in Sr_2RuO_4 as a function of the rotation angle of the muon about the fourfold axis through the apical O. Points represent the calculated energies, while the solid line represents the fourfold potential $V(\phi) = V_0[1 - \cos(4\phi)]/2$, with $V_0 = 70$ meV.

The endpoints of path P5 can be connected by traversing P1 followed by P4, and those of P4 by P1 followed by P5, as shown in Fig. S13(b). Since the barrier for P1 is very small, neither of the barriers for P4 and P5 can exceed the other, and hence they must be equal. The point marked Z in Fig. S13(b), at $(1/4, 1/4, 1/4)$ in the conventional cell, has symmetry $2/m$; its inversion center exchanges the ends of P5, and the twofold axis C_2 through it exchanges the ends of P4, so the force on a muon at Z vanishes by symmetry, making Z a natural candidate transition state for both paths. A relaxation with this symmetry imposed places Z 0.754 eV above site A. The muon-only Hessian at Z has a single imaginary mode, directed within 2° of the line joining the ends of P4, while the two remaining modes are again stiff (3.9 and 12.7 eV Å^{-2}), confirming that Z is the transition state of P4 and hence, by the earlier argument, sets the barrier for P5 too. At Z the muon sits 1.28 Å from each of two oxygens, so the stiff O–μ stretch of site A is lost and the ZPE falls to 0.530 eV, giving a corrected barrier for P4 and P5 of 0.366 eV.

The barriers for each of the candidate hopping paths are summarized in Table S4. The muon is free to move between the four symmetry-equivalent positions around the same apical oxygen, but every path to a different apical oxygen crosses a substantial barrier. The direct P3 path has a corrected barrier of 0.671 eV. However, its endpoints can alternatively be connected through two successive P4 hops via a copy of site A in the adjacent SrO layer. The ZPE correction reverses the energetic ordering of the two routes, because at Z the muon is shared between two oxygens and the stiff O–μ stretch is lost, whereas at Y it is bonded to a single equatorial oxygen and so retains a stretch of stiffness comparable to that at site A. The lowest effective barrier for motion between sites associated with different apical oxygen atoms is therefore 0.366 eV. Long-range diffusion is consequently negligible at the temperatures of our measurements. Long-range diffusion along c would additionally require the muon to pass through the RuO_2 layer. Site B is the only candidate site found in this layer and lies 0.978 eV above site A, so the barrier in this direction is likely to be at least this large.

For paths P1, P4 and P5 we calculated the energy profile along each path using the climbing-image nudged elastic band (NEB) method [19], with the band relaxed onto the minimum-energy path using the ODE12R adaptive-timestep scheme [20]. The resulting profiles are shown in Fig. S14. None shows an intermediate minimum, and each rises to a single maximum that coincides with the saddle identified above, X for P1 and Z for P4 and P5, with energies agreeing with the saddle-point relaxations to within 1 meV. At each maximum, the tangent to the band is parallel to the imaginary mode of the muon-only Hessian, confirming that this mode lies along the minimum-energy path. This is significant for P4 and P5, whose central image is held at Z by symmetry, so that the band alone could not have located the saddle. The energy profiles of P4 and P5 are indistinguishable because the two paths share almost their entire route: the muon rotates by 45° about the fourfold axis through its apical oxygen to X, crosses Z to the equivalent point on the adjacent apical oxygen, and then rotates by a further 45° to site A. P4 and P5 differ only in the sense of this final rotation, and these two final rotations are mirror images of each other through the plane m containing Z, so they have the same energy.

Along P1, the energy is a smooth function of the rotation angle ϕ of the muon about the fourfold axis through the apical oxygen (Fig. S15), with minima at $\phi = 0°$ and 90° and a single maximum at $\phi = 45°$ (X). It is well described by the simplest fourfold potential, $V(\phi) = \frac{1}{2}V_0(1 - \cos 4\phi)$ with V_0 equal to the barrier, which reproduces the calculated

TABLE S4. Muon hopping paths and the current best estimates of their energy barriers in Sr_2RuO_4. The length is the distance between the two muon sites, rather than the length of the minimum-energy path. The barriers are the energies of the saddle points X, Y and Z relative to site A. For P1, P4 and P5 the maxima of the climbing-image NEB bands agree with these to within 1 meV. The corrected barriers are obtained from Eq. (S5). The muon zero-point energy (ZPE) is lower at each saddle than at site A, which reduces each barrier by the difference. For P2, the listed barrier corresponds to each of the two successive P1 hops comprising this path.

Path	Length (Å)	Barrier (eV)	Saddle ZPE (eV)	Corrected barrier (eV)
P1	1.25	0.070	0.835	−0.013
P2	1.77	0.070	0.835	−0.013
P3	2.10	0.675	0.915	0.671
P4	2.23	0.754	0.530	0.366
P5	2.55	0.754	0.530	0.366

profile to within 9 meV, the barrier being slightly broader than this form. Since P2 comprises two successive P1 hops, the same profile, repeated every 90°, describes the full rotation of the muon about the apical oxygen. The zero-point energy of the bending mode along this rotation (0.137 eV, Table S3) is about twice the barrier, consistent with the vanishing corrected barrier.

D. Electronic contribution to the zero-field relaxation

Since the calculated nuclear contribution is both too weak and closer to a Gaussian-like relaxation, we next consider a dilute distribution of electronic moments. For a static dilute distribution of randomly located dipolar moments, the zero-field relaxation has the Lorentzian Kubo–Toyabe form [21, 22]

$$G(t) = \frac{1}{3} + \frac{2}{3}(1 - at)e^{-at} \simeq e^{-\Lambda t}, \qquad \Lambda = \frac{4a}{3}, \tag{S6}$$

where the exponential approximation applies at early times. For $\Lambda \simeq 0.04\ \mu s^{-1}$, the Lorentzian Kubo–Toyabe function is well approximated by an exponential over the experimental time window. For dilute moments,

$$a = \eta \frac{\mu_0}{4\pi} n c \mathrm{csc}\mu, \qquad \eta = 4.5406, \tag{S7}$$

where n_{cs} is the density of candidate sites, $c \ll 1$ is the fraction of those sites carrying a magnetic moment μ, and the remaining sites are nonmagnetic. Taking $\Lambda \simeq 0.04\ \mu s^{-1}$ gives $c\mu/\mu_B \simeq 8 \times 10^{-4}$. Thus, for moments of order $1\mu_B$, the corresponding magnetic-site concentration is of order $c \simeq 800$ ppm.

Such dilute electronic moments could be associated with Ru-site vacancies, antisite defects, or oxygen defects that polarize nearby Ru orbitals. In this picture, a nominally nonmagnetic structural defect can produce a spatially extended Ru spin polarization. One may further speculate that a defect at position $\boldsymbol{r}'$ locally suppresses superconductivity, so that $\Delta(\boldsymbol{r}) \to 0$ as $\boldsymbol{r} \to \boldsymbol{r}'$. The resulting low-energy quasiparticles could enhance the local density of states at E_F and, in turn, the local magnetic susceptibility, thereby slightly increasing the Ru spin polarization around the defect. This last step is a possible microscopic scenario rather than a conclusion of the present calculations.

[1] V. Grinenko, D. Das, R. Gupta, B. Zinkl, N. Kikugawa, Y. Maeno, C. W. Hicks, H.-H. Klauss, M. Sigrist, and R. Khasanov, *Unsplit superconducting and time reversal symmetry breaking transitions in Sr_2RuO_4 under hydrostatic pressure and disorder*, Nat. Commun. **12**, 3920 (2021). https://doi.org/10.1038/s41467-021-24176-8

[2] Y. Maeno, K. Yoshida, H. Hashimoto, S. Nishizaki, S. Ikeda, M. Nohara, T. Fujita, A. P. Mackenzie, N. E. Hussey, J. G. Bednorz, and F. Lichtenberg, *Two-Dimensional Fermi Liquid Behavior of the Superconductor Sr_2RuO_4*, J. Phys. Soc. Jpn. **66**, 1405–1408 (1997). https://doi.org/10.1143/JPSJ.66.1405

[3] A. Kanbayasi, *Magnetic Properties of $SrRuO_3$ Single Crystal*, J. Phys. Soc. Jpn. **41**, 1876–1878 (1976). https://doi.org/10.1143/JPSJ.41.1876

[4] A. Kanbayasi, *Magnetocrystalline Anisotropy of $SrRuO_3$*, J. Phys. Soc. Jpn. **41**, 1879–1883 (1976). https://doi.org/10.1143/JPSJ.41.1879

[5] S.-I. Ikeda, Y. Maeno, S. Nakatsuji, M. Kosaka, and Y. Uwatoko, *Ground state in $Sr_3Ru_2O_7$: Fermi liquid close to a ferromagnetic instability*, Phys. Rev. B **62**, R6089–R6092 (2000).
https://doi.org/10.1103/PhysRevB.62.R6089

[6] Alex Amato and Elvezio Morenzoni, *Introduction to Muon Spin Spectroscopy. Applications to Solid State and Material Sciences*, Springer Nature (2024).
https://doi.org/10.1007/978-3-031-44959-8

[7] A. Yaouanc and P. D. de Réotier, *Muon Spin Rotation, Relaxation, and Resonance*, Oxford Science Publications, 2011.

[8] S. J. Blundell, R. De Renzi, T. Lancaster, and F. L. Pratt (eds.) *Muon spectroscopy. An introduction*, Oxford: Oxford University Press, 2022.

[9] A. Schenck, *Muon Spin Rotation Spectroscopy: Principles and Applications in Solid State Physics*, Adam Hilger, Bristol, 1985.

[10] S. J. Clark, M. D. Segall, C. J. Pickard, P. J. Hasnip, M. I. J. Probert, K. Refson, and M. C. Payne, *First principles methods using CASTEP*, Z. Kristallogr. Cryst. Mater. **220**, 567–570 (2005).
https://doi.org/10.1524/zkri.220.5.567.65075

[11] J. P. Perdew, K. Burke, and M. Ernzerhof, *Generalized Gradient Approximation Made Simple*, Phys. Rev. Lett. **77**, 3865–3868 (1996).
https://doi.org/10.1103/PhysRevLett.77.3865

[12] Hk. Müller-Buschbaum and J. Wilkens, *Ein Beitrag über Sr_2RuO_4 und $Sr_3Ru_2O_7$ zur Oktaederstreckung von M^{4+} in K_2NiF_4- und $Sr_3Ti_2O_7$-Typ-Verbindungen*, Z. Anorg. Allg. Chem. **591**, 161–166 (1990).
https://doi.org/10.1002/zaac.19905910118

[13] H. J. Monkhorst and J. D. Pack, *Special points for Brillouin-zone integrations*, Phys. Rev. B **13**, 5188–5192 (1976).
https://doi.org/10.1103/PhysRevB.13.5188

[14] B. M. Huddart, A. Hernández-Melián, T. J. Hicken, M. Gomilšek, Z. Hawkhead, S. J. Clark, F. L. Pratt, and T. Lancaster, *MuFinder: A program to determine and analyse muon stopping sites*, Comput. Phys. Commun. **280**, 108488 (2022).
https://doi.org/10.1016/j.cpc.2022.108488

[15] B. M. Huddart, I. J. Onuorah, M. M. Isah, P. Bonfà, S. J. Blundell, S. J. Clark, R. De Renzi, and T. Lancaster, *Intrinsic nature of spontaneous magnetic fields in superconductors with time-reversal symmetry breaking*, Phys. Rev. Lett. **127**, 237002 (2021).
https://doi.org/10.1103/PhysRevLett.127.237002

[16] M. Gomilšek, F. L. Pratt, S. P. Cottrell, S. J. Clark, and T. Lancaster, *Many-body quantum muon effects and quadrupolar coupling in solids*, Commun. Phys. **6**, 142 (2023).
https://doi.org/10.1038/s42005-023-01260-7

[17] S. G. Kang and D. S. Sholl, *First principles studies of proton conduction in $KTaO_3$*, J. Chem. Phys. **141**, 024707 (2014).
https://doi.org/10.1063/1.4885851

[18] T. U. Ito, W. Higemoto, and K. Shimomura, *Understanding muon diffusion in perovskite oxides below room temperature based on harmonic transition state theory*, Phys. Rev. B **108**, 224301 (2023).
https://doi.org/10.1103/PhysRevB.108.224301

[19] G. Henkelman, B. P. Uberuaga, and H. Jónsson, *A climbing image nudged elastic band method for finding saddle points and minimum energy paths*, J. Chem. Phys. **113**, 9901–9904 (2000).
https://doi.org/10.1063/1.1329672

[20] S. Makri, C. Ortner, and J. R. Kermode, *A preconditioning scheme for minimum energy path finding methods*, J. Chem. Phys. **150**, 094109 (2019).
https://doi.org/10.1063/1.5064465.

[21] A. T. Fiory, *Muon-spin relaxation in systems of dilute dipolar impurities: Numerical treatment of fluctuations*, Hyperfine Interact. **8**, 777–780 (1981).
https://doi.org/10.1007/BF01037561

[22] G. A. Gist and S. A. Dodds, *Zero-field muon-spin-resonance linewidths in dilute magnetic alloys*, Phys. Rev. B **30**, 2340–2344 (1984).
https://doi.org/10.1103/PhysRevB.30.2340